International Journal of Biological Macromolecules 253 (2023) 126763

Contents lists available at ScienceDirect

International Journal of Biological Macromolecules

journal homepage: www.elsevier.com/locate/ijbiomac

Structural and computational insights into the regioselectivity of SpnK involved in rhamnose methylation of spinosyn

Shuxin Huang [a], Huining Ji [b], Jianting Zheng [a,b,*]

[a] State Key Laboratory of Microbial Metabolism, School of Life Sciences and Biotechnology, Shanghai Jiao Tong University, Shanghai 200240, China
[b] Joint International Research Laboratory of Metabolic & Developmental Sciences, Shanghai Jiao Tong University, Shanghai 200240, China

ARTICLE INFO

Keywords:
Methyltransferase
Regioselectivity
Crystal structure
Molecular dynamics simulation
Spinosyn

ABSTRACT

Rhamnose methylation of spinosyn critical for insecticidal activity is orchestrated by substrate specificity of three S-adenosyl-L-methionine (SAM) dependent methyltransferases (MTs). Previous *in vitro* enzymatic assays indicate that 3′-O-MT SpnK accepts the rhamnosylated aglycone (RAGL) and 2′-*O*-methylated RAGL as substrates, but does not tolerate the presence of a methoxy moiety at the O-4′ position of the rhamnose unit. Here we solved the crystal structures of *apo* and ligand-bound SpnK, and used molecular dynamic (MD) simulations to decipher the molecular basis of substrate specificity. SpnK assembles into a tetramer, with each set of three monomers forming an integrated substrate binding pocket. The MD simulations of SpnK complexed with RAGL or 2′-*O*-methylated RAGL revealed that the 4′-hydroxyl of the rhamnose unit formed a hydrogen bond with a conserved Asp299 of the catalytic center, which is disrupted in structures of SpnK complexed with 4′-*O*-methylated RAGL or 2′,4′-di-*O*-methylated RAGL. Comparison with SpnI methylating the C2′-hydroxyl of RAGL reveals a correlation between a DLQT/DLWT motif and the selectivity of rhamnose O-MTs. Together, our structural and computational results revealed the structural basis of substrate specificity of rhamnose O-MTs and would potentially help the engineering of spinosyn derivatives.

1. Introduction

Methyltransferases (MTs) participate in specialized metabolic pathways by transferring a methyl moiety from a donor, in most cases, S-adenosyl-L-methionine (SAM), to an accepter molecule [1]. MTs have a wide range of substrate scope including small molecule natural products like primary or secondary metabolites, and macromolecular substrates like DNA, RNA, or proteins [2–4]. MTs are categorized according to the nucleophile accepter such as oxygen, nitrogen, carbon, or sulfur [5]. It has been reported that some methyltransferases utilize a metal ion to aid in the binding of substrates *via* interacting with hydroxyl groups. In catechol *O*-methyltransferases (COMT), a Mg^{2+} ion is required to bind and orient two catechol hydroxyl groups [6]. In caffeoyl-CoA *O*-methyltransferase (CCoAOMT), the deprotonation of caffeoyl 3′-OH as well as the maintenance of the proximity of oxoanion and the SAM methyl group are facilitated by a Ca^{2+} ion [7]. Engineered methionine adenosyltransferase can utilize L-Met analogs and adenosine triphosphate (ATP) to synthesize SAM analogs, which enables the SAM-dependent MTs to introduce various non-native alkyl groups into DNA, proteins, or natural products [8–10].

O-Methylation can protect the reactive hydroxyl moieties from undesired modification by masking peripheral hydroxyl groups, and result in dramatic change in biochemical and pharmacological properties of chemical compounds. Notably, methylation of unbound hydroxyl groups can significantly improve the metabolic stability and increase membrane permeability, thereby promoting the absorption, oral bioavailability, bioactivity, and reactivity of acceptor molecules [11,12]. To expand the structural diversity and facilitate the chemoenzymatic synthesis of novel complex natural products, it is important to study and utilize the substrate selecting rules of O-MTs that are responsible for modifying of deoxysugar moieties.

Spinosad, a prominent bio-pesticide, comprises spinosyn A and spinosyn D as major and minor components within the spinosyn family. These components are derived from the secondary metabolites of the soil actinomycete *Saccharopolyspora spinosa* and effectively target insect nicotinic acetylcholine receptors [13,14]. Spinosyn is composed of a polyketide aglycone and two sugars, forosamine and tri-*O*-methyl-rhamnose. Spinosyns are produced through a biosynthetic pathway

* Corresponding author at: State Key Laboratory of Microbial Metabolism, School of Life Sciences and Biotechnology, Shanghai Jiao Tong University, Shanghai 200240, China.
E-mail address: jtzheng@sjtu.edu.cn (J. Zheng).

https://doi.org/10.1016/j.ijbiomac.2023.126763
Received 16 July 2023; Received in revised form 3 September 2023; Accepted 4 September 2023
Available online 11 September 2023

involving polyketide synthases (PKS) SpnA, SpnB, SpnC, SpnD and SpnE that generate the macrolide. Various post-PKS enzymes SpnF, SpnJ, SpnL and SpnM decorates tetracyclic core to introduce diverse structural and functional activities. The SpnN, SpnO, SpnQ, SpnS and SpnR participate in the synthesis and attachment of forosamine [15]. Rhamnose is attached to the aglycone through the catalysis of glycosyltransferase SpnG and subsequently tri-*O*-methylated by SpnI, SpnK and SpnH [16].

An artificial neural networks-based quantitative structure activity relationships study has led to the discovery of spinetoram, which is a second-generation spinosyn insecticide. The study involves extending the rhamnose 3′-O-alkyl group a methyl to ethyl moiety and the saturating the 5,6-double bond of the macrolide [17]. 3′-O-ethylation leads to improved lepidopteran activity and enhanced insecticidal activity toward pests including two-spotted spider mites and cotton aphids with the cost of the ultraviolet stability. However, the hydrogenation of double bond between C5 and C6 of macrolide leads to an increased melting point, thereby restoring the ultraviolet stability. Spinetoram offers superior efficacy, longer control duration and expanded spectrum compared with spinosad, while maintaining spinosad's highly favorable environmental profile [18].

Based on *in vitro* studies, *O*-methylation of the rhamnose in spinosyn biosynthesis pathway is performed in the order of SpnI, SpnK and SpnH [16] (Scheme 1). They are proposed to methylate the C2′-, C3′-, and C4′-hydroxyl groups of the rhamnose moiety sequentially [15]. Among the three possible di-*O*-methylated-RAGL (**IV**, **V**, **VI**), only 2′,3′-di-*O*-methylated-RAGL (**IV**) can be converted to 2′,3′,4′-tri-*O*-methylated-RAGL (**VII**) by SpnH, suggesting that SpnH is responsible for the last methylation step. Actually, SpnH is very promiscuous and also processes RAGL, 2′-*O*-methylated-RAGL (**I**) and 3′-*O*-methylated-RAGL (**II**). Both SpnI and SpnK can converted RAGL to corresponding monomethylated products (**I** and **II**). However, only 2′-*O*-methylated-RAGL (**I**) can be further converted to 2′,3′-di-*O*-methylated-RAGL (IV) by SpnK. Obviously, the substrate specificity of SpnK and SpnI controls the sequence of methylation reactions, but the molecular basis is still obscure. Here, we solved crystal structures of SpnK and used molecular dynamic (MD) simulations to provide detailed molecular insights into substrate recognition of rhamnose O-MTs.

2. Materials and methods

2.1. Cloning, expression, and purification of SpnK

Amplification of *spnk* gene from genomic DNA of *S. spinosa* NRRL18395 was achieved *via* the use of forward primer 5′-ATCGTAATCCATATGTCCACAACGCACGAGATCGAAAC-3′ and reverse primer 5′-TGATTCGATGAATTCACTCGTCCTCCGCGCTGTTCA-3′. Subsequently, the amplicon was inserted into the *Nde* I/*EcoR* I sites of pET28a (+) vector (Novagen). The resulting expression plasmid was subsequently introduced into expression host *Escherichia coli* BL21(DE3) and then cultured in 8 mL LB culture containing 50 μg/mL kanamycin for 6 h followed by inoculation into 1 L of LB containing 50 μg/mL kanamycin followed by incubation at 37 °C until OD_{600} of 0.6 was achieved. The culture was then subjected to a temperature reduction to 16 °C when 0.5 mM inducer, isopropyl β-D-thiogalactopyranoside, was introduced. After an additional 14 h of growth in 16 °C, cells were collected *via* centrifugation (4500 *g* for 7 min) and resuspended in lysis buffer (50 mM Tris, pH 7.5, 10 mM $MgCl_2$, 500 mM NaCl) for sonification. Resulting lysate was centrifugated (15000 g for 40 min). Supernatant was applied to a Ni-NTA column. Elution of SpnK was

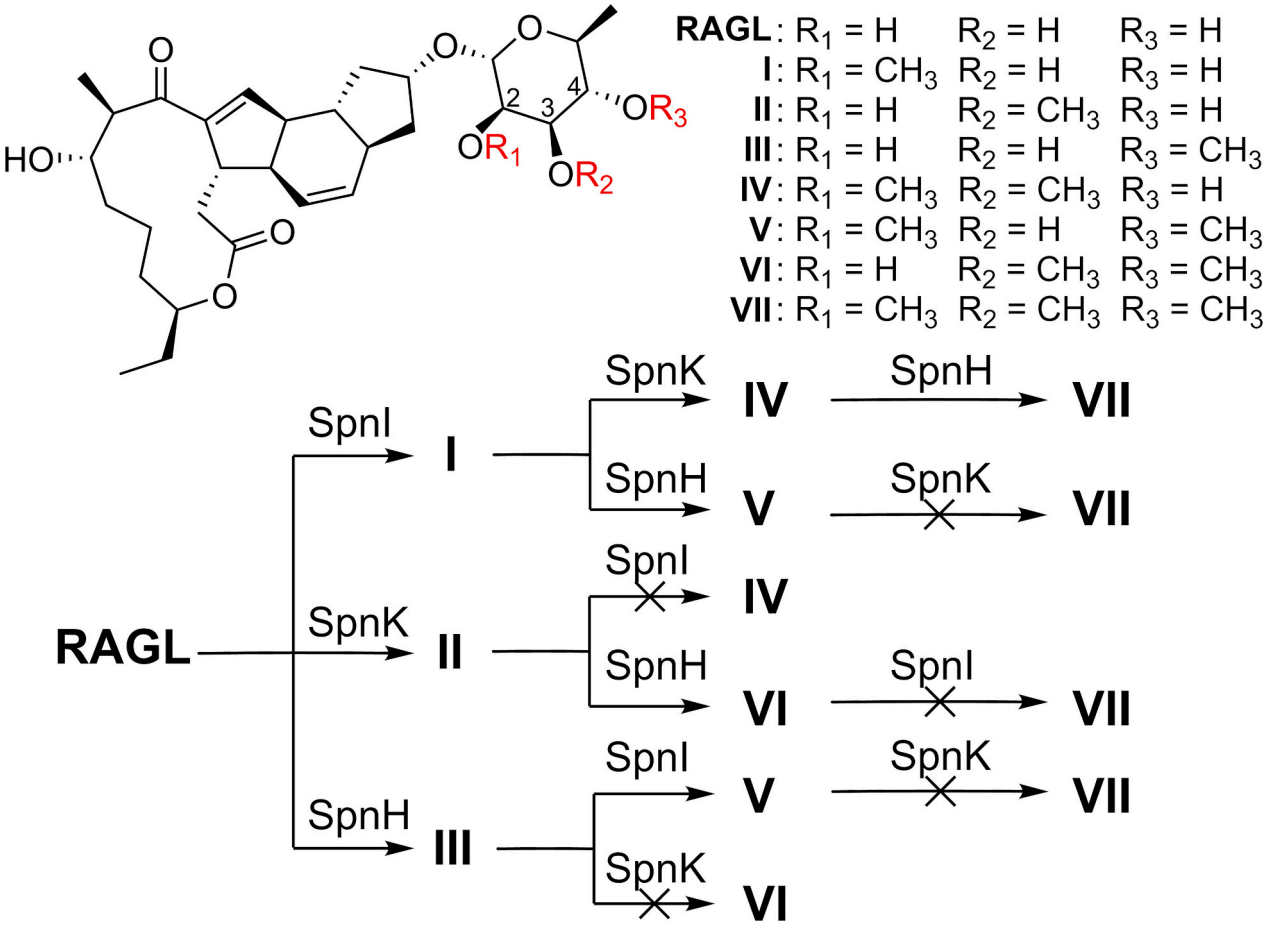

Scheme 1. Methylation sequences of rhamnose of spinosyn.

accomplished with lysis buffer containing 300 mM imidazole and subsequent purification was carried out using a Superdex 200 gel filtration column equilibrated with 2 mM $MgCl_2$, 150 mM NaCl and 10 mM Tris (pH 7.5). Final concentration of SpnK was achieved using protein concentrator and adjusted to 20 mg/mL in 2 mM $MgCl_2$, 30 mM NaCl and 10 mM Tris (pH 7.5) before flash-freezing and storage at −80 °C for later use.

2.2. Crystallization, data processing and structure determination

Crystals were grown at 20 °C over a two-week period using sitting-drop vapor-diffusion method. The drops were prepared by combining SpnK (20 mg/mL) and crystallization buffer (100 mM sodium citrate, pH 6.3, 34 % *v*/v PEG 200) in a 2:1 ratio. The growth of SpnK-SAH crystals in the presence of 3 mM SAH was carried out using the same condition as for unliganded SpnK crystals. Crystals were rapidly frozen in liquid nitrogen before collecting data. Diffraction data for both SpnK and SpnK-SAH complex were collected at beamline BL18U1 of the Shanghai Synchrotron Radiation Facility and processed using HKL2000. The molecular replacement technique, using the monomer of the mycinamicin VI 6-deoxyallose 2′-*O*-methyltransferase, MycE (PDB code 3SSO), which shares 45 % sequence identity with SpnK, was used to solve the phase of unliganded SpnK in the Phaser program of CCP4. The refinement process was carried out using Coot and Refmac5 with default NCS restraints [19,20]. SpnK-SAH structure was determined by molecular replacement utilizing *apo* SpnK structure. The protein figures were generated using ChimeraX [21] and PyMOL [22].

2.3. Model building using AlphaFold

Structure of SpnI was predicted through recently released AlphaFold-Multimer using Shanghai Jiao Tong University's supercomputing resources [23]. AlphaFold employed the deep learning algorithm for protein structure prediction, so only protein sequence (GenBank ID: AAG23270.1) was submitted. It was then superimposed on the tetramer structure of SpnK-SAH with PyMOL to generate the complete structure of SpnI-SAM with ligand and magnesium.

2.4. Preparing SpnK-SAM-substrate complexes

In order to determine the SpnK-SAM complex structure, SAM was docked into the active site guided by the structure of SpnK-SAH. Complete active sites formed by three monomers of SpnK or SpnI, one SAM and one magnesium were chosen as receptor. Structures of the ligand **I**, **II**, **III**, **V** and RAGL were prepared using Chemdraw 19.0 and then changed into their 3D PDB structures using Chem3D 19.0. AutoDock Tool 1.5.6 was employed to eliminate unbound water molecules and introduce hydrogen atoms and charges to generate the pdbqt files of protein and ligands. AutoDock Vina 1.1.2 docked the ligands toward the receptors [24]. The molecular conformation provided by AutoDock Vina with lowest docking energy was selected for molecular dynamics (MD) simulations.

2.5. Molecular dynamics simulations

The protonation state of the SpnK and SpnI residues at pH 7.5 was determined using the H++ web server and then followed by visual inspection [25]. The conformation of catalytic His273, specifically the rotation of its imidazole ring, is regulated by the influence of two hydrogen bonds formed with the neighboring water. In the process of methylation, His273 serves as a general base, with NE1 of histidine initiating deprotonation of the hydroxyl group in the initial step. To mimic the pre-reaction state where histidine is deprotonated and the hydroxyl group remains protonated, His273 was configured as deprotonated with a hydrogen attached to the delta nitrogen (HID). To optimize the conformation of substrates, a restrained electrostatic potential (RESP) charge fitting procedure was used to assign partial charges to the substrates with missing parameters produced by the Antechamber package, and Gaussian 09 was employed at the HF/6-31G(d) level of theory [26,27]. MD simulations were carried out utilizing AMBER software package (version 18) for the SpnK-**I**, SpnK-RAGL, SpnK-**III**, SpnK-**V**, SpnI-RAGL and SpnI-**II** complexes [28]. The Amber ff14SB and general Amber force field (GAFF) were employed for proteins and the substrates, while the TIP3P model was performed to solvent molecules to parameterize all molecules of the complex [29]. The Particle Mesh Ewald (PME) method was performed to treat long-range electrostatic interactions, and the SHAKE algorithm was utilized to constrain bonds that involve hydrogen atoms [30,31]. Whole system was inserted in a cubic box containing solvent molecules and sodium ions were introduced to neutralize the system. The above-prepared system was subjected to a two-stage energy minimization combining steepest descent algorithm and conjugate gradient, ensuring that steric clashes or inappropriate geometry had been eliminated from the solvated system. The system was heated from 0 to 300 K with fixed heavy atoms in 50 ps. A short 50 ps MD simulation was performed at 300 K to get a proper density followed by 1 ns equilibration under NPT condition. A 50 ns MD production simulation was finally carried out under NPT conditions without any restraints. Each system performed three-times simulations with different random numbers. Six 200 ns simulation were carried out by extending short simulations of the best trajectory of each system. CPPTRAJ was used for analyzing the MD trajectories, and VMD was employed for visual inspection [32,33]. The root mean-square deviation (RMSD) of the system was calculated using Cα atoms. Clustering based on RMSD was carried out using diffusely accepted average linkage clustering algorithms, and characteristic structures were abstracted to display substrate conformation changes. Then hydrogen-bonding analysis was performed to the MD simulation trajectories with an acceptor-donor-hydrogen angle greater than 135° and donor-acceptor distance of less than 3.0 Å.

2.6. Bind free energy calculations

Using the classical simulation technique of molecular mechanics Poisson-Boltzmann surface area (MM-PBSA), the binding affinity between the proteins and different substrates was evaluated. In this study, the MMPBSA.py module of Amber 18 was performed to calculate the Gibbs free energy of binding of simulated SpnK-**I**, SpnK-RAGL, SpnK-**III**, SpnI-RAGL and SpnI-**II** complexes, which were carried out by extracting 750 frames from the final 50 ns of MD trajectories through CPPTRAJ [34]. In the calculation of MMPBSA [35], the binding free energy of the interaction can be expressed as following Eq. (1):

$$\Delta G_{binding} = G_{complex} - \left(G_{protein} + G_{ligand}\right) \quad (1)$$

Here, $G_{complex}$ denotes the overall binding energy of protein-ligand complex, whereas $G_{protein}$ and G_{ligand} stands for the individual free energies of protein and ligand, respectively. The free energy of each component can be computed using following Eq. (2):

$$G_x = E_{MM} + G_{solvation} \quad (2)$$

In Eq. (2), x can refer to the complex, protein or ligand. E_{MM} represents bonded interactions (E_{bonded}) and non-bonded interactions ($E_{non-bonded}$) such as van der Waals interaction (E_{vdw}) and electrostatic interactions (E_{ele}) in a vacuum.

$$E_{MM} = E_{bonded} + E_{non-bonded} = E_{bonded} + E_{vdw} + E_{ele} \quad (3)$$

The free energy of solvation ($G_{solvation}$) accounts for the combination of polar (G_{PB}) and non-polar (G_{SA}) contributions to solvation energy and is expressed as Eq. (4):

$$G_{solvation} = G_{PB} + G_{SA} \quad (4)$$

3. Results

3.1. Overall structure of SpnK

SpnK was heterologously expressed in *E. coli* and purified to homogeneity by immobilized metal affinity chromatography (IMAC) and size exclusion chromatography (Fig. S1). SpnK crystals were obtained by matrix screens and grown in a solution containing 100 mM sodium citrate, pH 6.3 and 34 % v/v PEG 200 (Fig. S1c). Complex crystals of SpnK-SAH were obtained by supplementing SAH to the protein. Thus, we obtained the crystal structures of SpnK in two forms: *apo* SpnK at 2.5 Å and SpnK-SAH at 2.1 Å (Table 1). Both crystals contain two SpnK molecules in an asymmetric unit, poised to create a homotetrameric assembly through 422-symmetry (Fig. 1). The overall conformations of SpnK and SpnK-SAH are essentially the same, except that the missing loop between α8 and β6 in C-terminal MT domain becomes ordered upon the binding of SAH. The SpnK-SAH complex was used in the following structural analysis due to the higher resolution.

Each SpnK monomer contains two domains including C-terminal catalytic MT domain (C-MT, residues 159–386) and N-terminal auxiliary domain (N-AD, residues 5–152) (Fig. 1b). The MT domain follows the common structural pattern of Class I SAM-dependent methyltransferase, characterized by central seven-stranded β-sheet with three helices on both sides. N-terminal auxiliary domain, which is absent in most MTs, contains a five-strand antiparallel β-sheet packing against five helices. A structural similarity search was conducted with SpnK monomer utilizing DALI server [36] and revealed that SpnK shows overall similarity to SAM/Metal-dependent MTs (Fig. S2). SpnK most closely resembles MycE from *Micromonospora griseorubida* (PDB ID 3SSO, 1.7 Å RMSD for 380 Cα atoms, 45 % sequence identity), which also has the N-terminal auxiliary domain [37]. Other homologous structures only contain the MT domain, including catechol O-MT domain (SH3-588 from *Rattus norvegicus*, PDB ID 7UD6, 2.9 Å RMSD for 158 Cα atoms,12 % sequence identity [38]; StrAOMT from *Streptomyces avermitilis*, PDB ID 8C9V, 2.8 Å RMSD for 163 Cα positions, 14 % sequence identity [39]; DesAOMT from *Desulfuromonas acetoxidans*, PDB ID 8C9T, 3.3 Å RMSD for 171 Cα atoms, 16 % sequence identity [39]), and SAM-dependent O-MT PaMTH1 from *Podospora anserina* (PDB ID 4YMG, 3.5 Å RMSD for 167 Cα positions, 14 % sequence identity) (Table S1) [40].

Crystallographic two-fold symmetry results in the formation of a tetramer, correlating with the molecular size determined by size-exclusive chromatography (Fig. S1b). The tetramer architecture has also been observed in MycE. In the asymmetric unit, the auxiliary domain of monomer A interacts with first two helices of the MT domain of monomer B, and *vice versa*, with a buried surface area of 1270 $Å^2$ (Fig. S3). Monomer A forms a head-to-tail dimer with its symmetry mate (designated as monomer A'), burying a surface area of 1623 $Å^2$. Monomer A makes contacts with the symmetry mate of monomer B (designated as monomer B') by the C-terminal MT domain, with a buried surface area of 1932 $Å^2$. Consequently, central seven-stranded β-sheets of monomer A and monomer B' are connected. The six interfaces (A-B, A-A', A-B', B-A', B-B' and A'-B') between the four monomers bury a total area of 9652 $Å^2$, involving 28 salt bridges, 80 hydrogen bonds and more than 900 non-bonded contacts.

Table 1
Summary of data collection, phasing, and refinement statistics for the crystal structures SpnK and SpnK-SAH.

	SpnK	SpnK-SAH
Data collection		
Wavelength (Å)	0.97915	0.97915
Space group	$P4_32_12$	$P4_32_12$
a, b, c (Å)	134.11 134.11 159.72	133.98 133.98 160.11
Resolution (Å)	50–2.50 (2.54–2.50)	50–2.10 (2.14–2.10)
R_{merge}	0.129 (0.796)	0.097 (0.898)
$<I/\sigma I>$	22.3 (4.3)	28 (3.2)
Completeness (%)	99.8 (97.5)	99.9 (96.1)
Multiplicity	11.5 (11.9)	12.6 (12.8)
Refinement statistics		
Resolution (Å)	50–2.50	50–2.10
No. of reflections	47,477	80,023
R_{work}/R_{free}	0.208/0.243	0.219/0.235
No. of atoms		
Protein	5869	5924
Mg^{2+}	2	2
SAH	0	52
Water	155	358
B factor ($Å^2$)		
Protein	43.2	31.8
Ligand	30.0	56.1
Water	28.2	30.0
RMSD		
Bond lengths (Å)	0.013	0.012
Bond angles (°)	1.63	1.70
Ramachandran plot (%)		
Favored	95.86	98.16
Allowed	4.01	1.84
Outliers	0.13	0.00

3.2. SAH binding in SpnK

Four active sites are formed in the tetramer, each involving three monomers. For example, the active site "A" is formed by N-AD of the monomer A, C-MT of monomer B, and C-terminal loop of monomer A'. Each SAH bound at the active site displays clear electron density (Fig. 2). As shown in Fig. 2b, the positively charged SAH cofactor is positioned in a negatively charged cleft, which is at the C-terminal of the C-MT β1 and almost perpendicular to the central seven-stranded β-sheet. The adenine is accommodated in a pocket formed by residues Ile198, Met228, Val230, Asp247, Gln248, Ser249, His277 and Ser272. Asp247 side chain forms a hydrogen bond with the adenine NH_2 at C6, while the backbone NH of Gln248 forms another hydrogen bond with the N1 of the adenine ring (Fig. 2c). The ribose is enfolded by Gly199, Tyr203, Asp229, Phe231 and Gly271. Hydrogen bonds are formed between the C3-OH of the ribose and the Gly201 and Tyr203 backbones. The side chain of Tyr203 acts like a lid covering the ribose. The carboxyl group of the SAH amino acid moiety interacts with Lys170 and Thr168 side chains by hydrogen bonds, whereas the amino group interacts with both Glu197 and Gly199. These protein-cofactor interactions may control the binding of the SAM in the cleft and orient the activated methyl group toward the C-terminal strand of the central seven-stranded β-sheet.

In the *apo* MycE structure (PDB ID 3SSO), the octahedral coordination of Mg^{2+} is formed by Asp275, Asp 304, Glu303 and three water molecules. Upon docking of mycinamicin-VI (PDB ID 3SSN), Mg^{2+} moves ~1 Å toward mycinamicin-VI. 2′- and 3′-OH of 6-deoxyallose coordinate with Mg^{2+} instead of two water molecules, and the interaction of Glu303 is replaced by a water molecule [37]. In SpnK, Mg^{2+} is also observed to interact with two conserved aspartates, Asp270 and Asp299 along with Asp169 and two water molecules. The similar active site organization of MycE suggests that SpnK employs a similar catalytic mechanism. Specifically, during the reaction, His273 functions as a base, deprotonating the 3′-OH of rhamnose, and then the resulting 3′-oxyanion performs nucleophilic attack on activated methyl group of the methyl donor SAM, thereby completing this reaction (Scheme 2).

3.3. MD simulations of docked SpnK-substrate complexes

According to previous *in vitro* assays, SpnK can methylate RAGL and 2′-*O*-methylated RAGL (**I**). Both substrates were docked into a SpnK

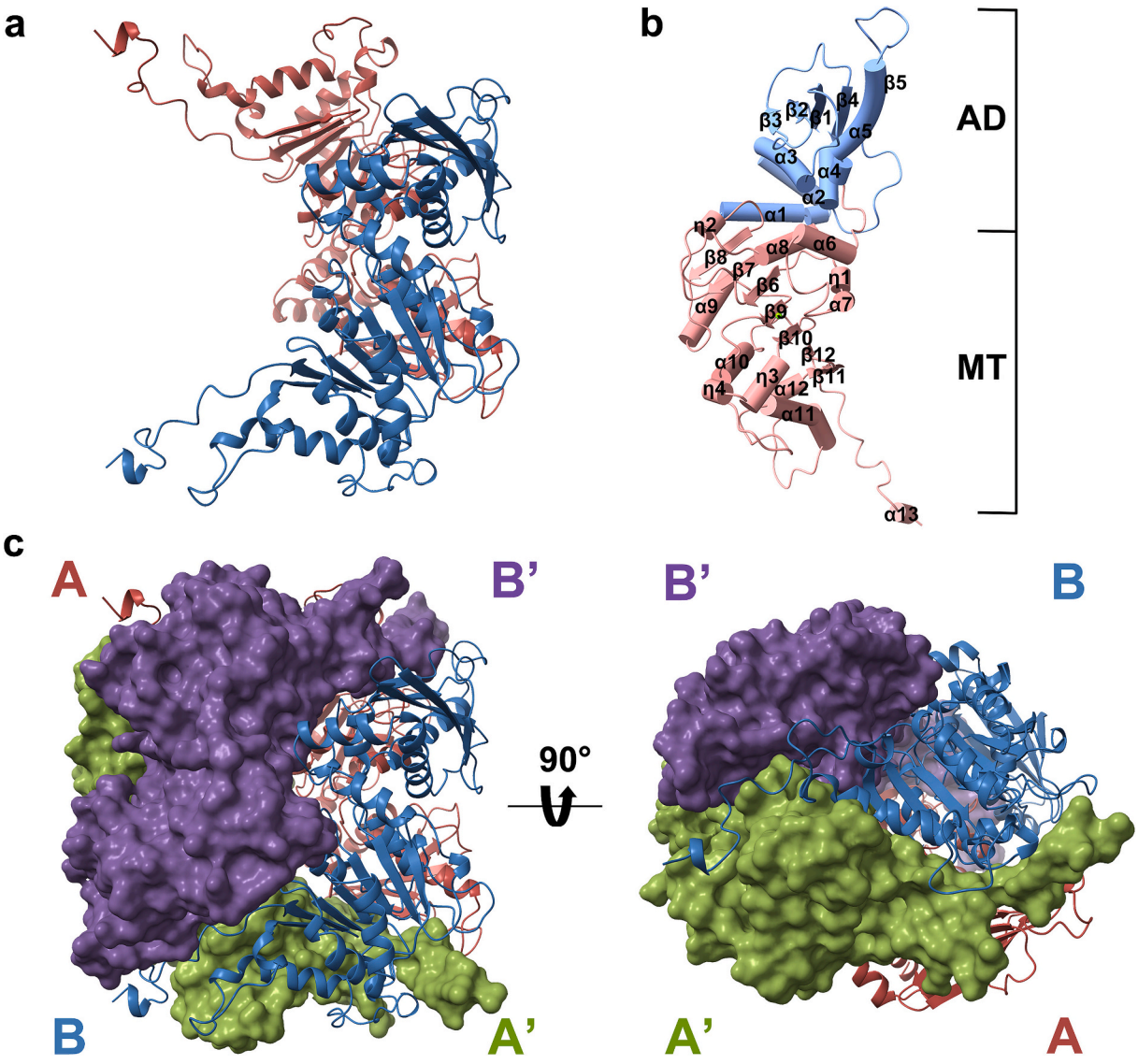

Fig. 1. Overall structure of SpnK. (a) Dimer of SpnK in an asymmetric unit. (b) SpnK monomer. α helices are drawn as cylinders. Secondary structure elements of SpnK are labeled. Auxiliary domain (colored blue) as well as methyltransferase domain (colored red) are indicated on the right. (c) Two views of SpnK tetramer in cartoon and surface representations. The four monomers, chain A, B, A' and B' are shown in red, blue, green, and purple.

active site to visualize the catalytic tendencies of SpnK. Docking energies ranged between −10.4 kcal/mol and −8.4 kcal/mol for RAGL, and between −9.4 kcal/mol and −8.5 kcal/mol for **I**. Molecular dynamic (MD) simulations were conducted to confirm substrate-enzyme interactions. The initial structures were selected from the conformations with lowest docking energies. The MD simulations were conducted for 200 ns. The stability of the MD systems was evaluated based on RMSD and RMSF analysis (Fig. S4). Emphasis was laid on the molecular interactions between rhamnosyl group and SpnK active site residues. Bound structures of RAGL and **I** are shown in Fig. 3. RAGL and **I** are nested similarly in the hydrophobic pocket composed of Val378 of chain A', Pro135 and Leu138 and Phe142 of chain A and Trp301 of chain B (Fig. 3). Besides, Val374 of chain A' and Leu174 of chain B also participate in the formation of the pocket accommodating **I** (Fig. 3b). A hydrogen bond is formed between the 4′-OH of RAGL and the side chains of the active site Asp299, and help orient 3′-OH toward the side chain NE2 of catalytic His273 (Fig. 3c). The hydrogen bond is observed in 56.9 % frames of SpnK-RAGL complex (Table S2). Interestingly, 98.0 % frames of SpnK-**I** complex contain the corresponding hydrogen bond (Fig. 3d) and the distance between the NE2 of catalytic histidine (His273) and the hydrogen of 3′-hyroxyl group (*d1*) in SpnK-**I** (2.19 ± 0.24 Å) is shorter than that in SpnK-RAGL (3.58 ± 0.81 Å), consistent with the observation that SpnK may prefer **I** to RAGL (Table S3).

SpnK does not accept **III** and **V**. Docking of **III** and **V** showed similar binding poses as the two native substrates except that the docking energy was slightly higher ranging between −10.3 kcal/mol and −7.4 kcal/mol for **III**, and between −9.0 kcal/mol and −8.1 kcal/mol for **V**. The MD simulations of SpnK-**III** and SpnK-**V** complex showed that the rhamnosyl groups flipped back toward the active site, resulting in longer *d1* (8.39 ± 3.36 Å in SpnK-**III** complex and 5.04 ± 0.61 Å in SpnK-**V** complex). Residues forming hydrophobic interactions were also fewer compared with the native substrates (Fig. 4). The methyl group of the 4′-oxygen disrupts the hydrogen bond with Asp299. Instead, carboxyl group of Asp299 forms a new hydrogen bond with 3′-OH of **III** and **V** (Fig. 4c, d). The new hydrogen bond is observed in 95.7 % frames of SpnK-**III** complex and in 97.9 % frames of SpnK-**V** complex, respectively. A hydrogen bond between Trp301 and 3′-OH of **III** or **V** is also observed in 13.4 % and 36.7 % frames, respectively. The two hydrogen bonds exist simultaneously in 12.9 % frames of SpnK-**III** complex and 36.2 % frames of SpnK-**V** complex.

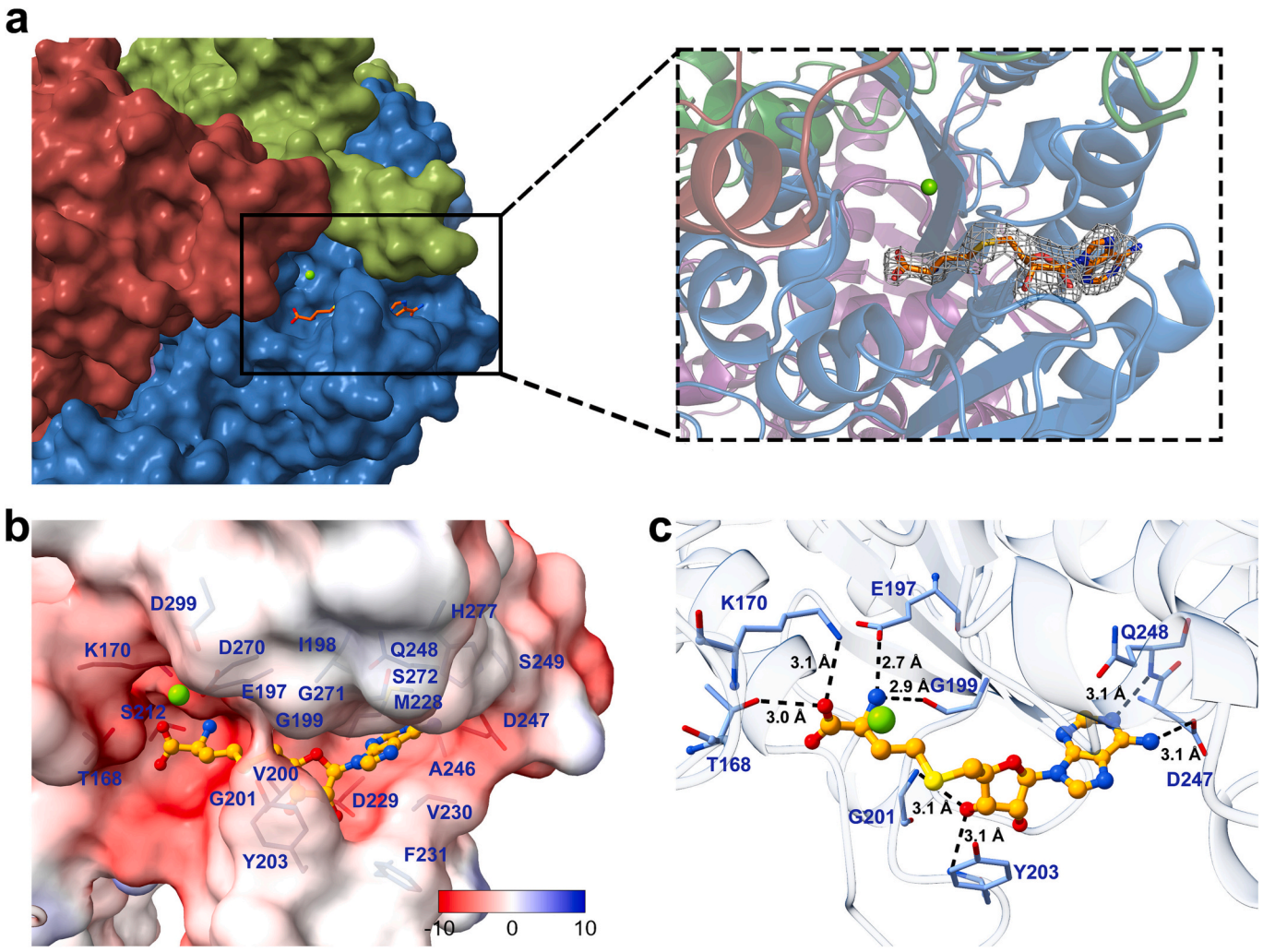

Fig. 2. Active site structure of SpnK. (a) An active site is composed of monomers A, B and A' (colored red, blue and green, shown as surface). The catalytic site is located on chain B. AD domain of chain A and C-terminal loop of chain C also contribute to the formation of the substrate binding pocket. Color is as in Fig.1(c). The close-up view of active site shows SAH omit Fo-Fc map contoured at 2.5σ. (b) Electrostatic potential surface diagram of the SAH binding pocket is displayed, where positive and negative potentials are displayed in blue and red, respectively. Residues participate in formation of SAH binding pocket are shown as sticks. SAH is shown as ball and stick model. (c) Residues form hydrogen bonds with SAH are colored blue and black dashed lines are utilized to indicate the hydrogen bonds.

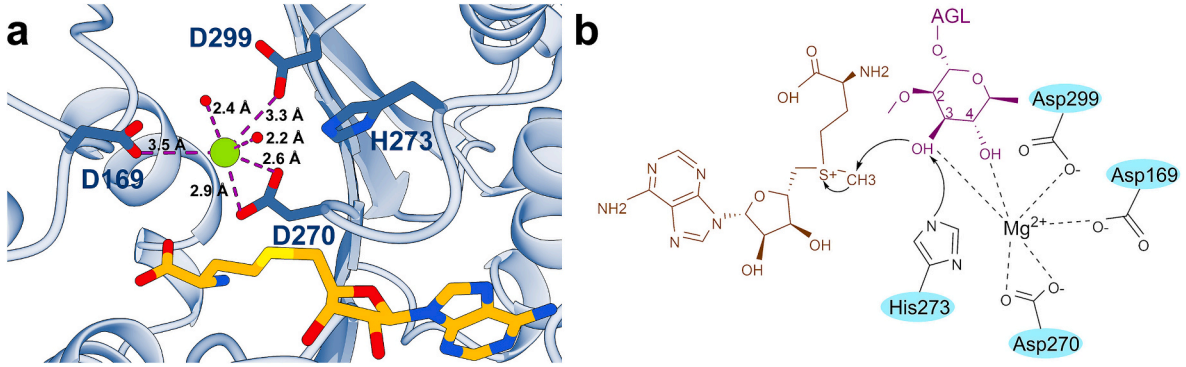

Scheme 2. Octahedral coordination of the magnesium (a) and the proposed catalysis mechanism of SpnK (b).

3.4. Comparison with SpnI

SpnI could methylate RAGL instead of **II**. SpnI also belongs to the MycE/TylE family, using a histidine as the catalytic residue. The attempts to solve the crystal structure of SpnI were unsuccessful. Therefore, a model of SpnI homoteramer was built through AlphaFold. As expected, SpnI has a nearly identical active site arrangement as SpnK (Fig. 5). SAM was modeled into the SpnI active site according to the SpnK-SAH crystal structure. RAGL and **II** were docked into SpnI active site with the energy of −9.5 kcal/mol to −8.2 kcal/mol and −9.1 kcal/mol to −7.8 kcal/mol, respectively. The docking poses of two substrates were slightly different from the substrates of SpnK. MD simulations were

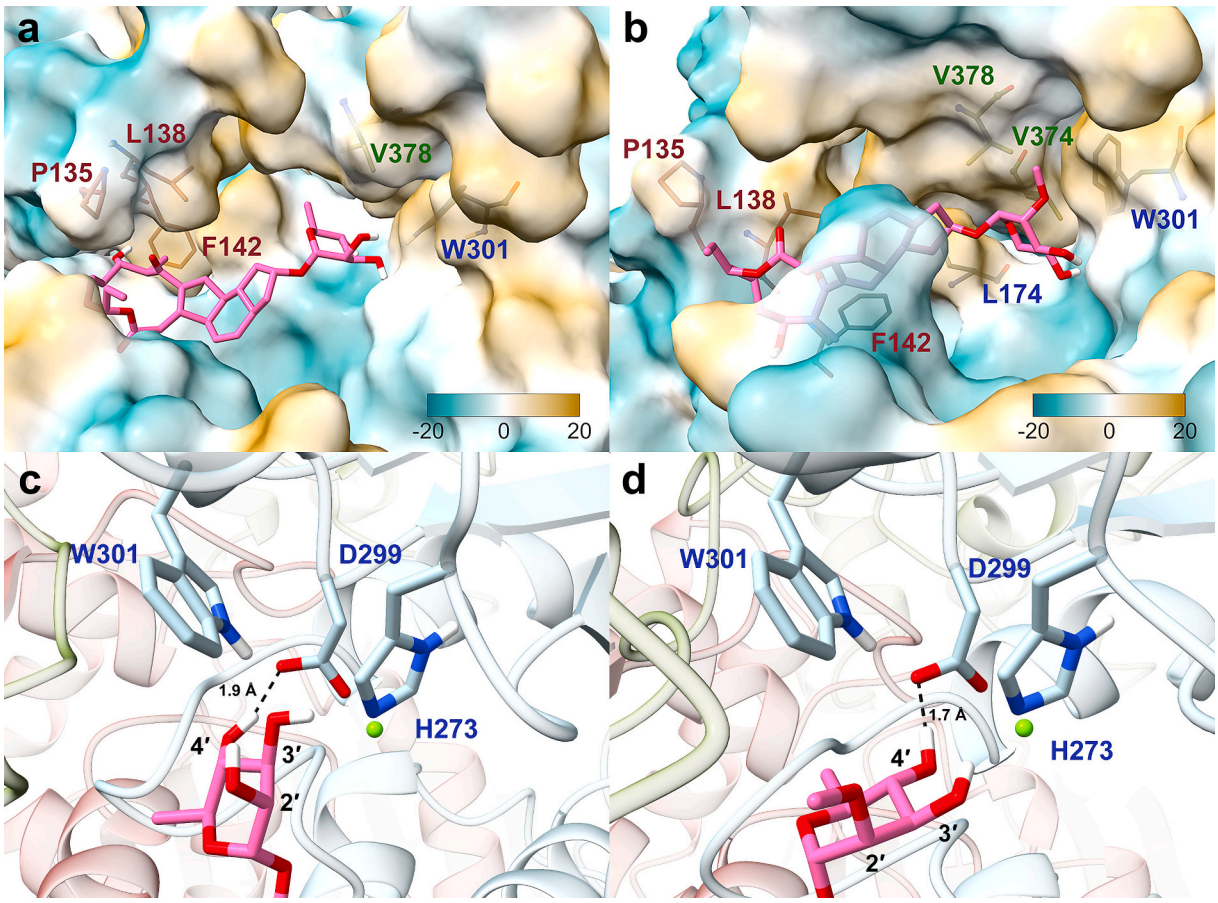

Fig. 3. MD simulations of SpnK and native substrates. (a, b) Hydrophobicity surface representation of RAGL (a) and **I** (b) binding pocket. Residues participated in hydrophobic interactions are depicted as sticks. RAGL and **I** are shown in magenta sticks. (c, d) Residues involved in substrate RAGL (c) and **I** (d) recognition are depicted as sticks, hydrogen bonds are donated by black dashed lines.

performed for the two SpnI complexes (Fig. S5). The rhamnose moiety of RAGL is stabilized by a hydrogen bond between the conserved Asp306 and 3′-OH in 98.4 % frames. In addition, the hydrogen bond between Gln308, corresponding to Trp301 of SpnK, and 4′-OH is observed in of 50.1 % frames (Fig. 5d). The hydrogen bonds between **II** and SpnI active site residues are drastically different. A hydrogen bond is formed between Asp306 and 2′-OH of **II** in 76.2 % frames (Fig. 5e, Table S4). Both the distance between the NE2 of catalytic histidine (His280) and the hydrogen of 2′-hyroxyl group (*d3*) and the distance between the oxygen of 2′-hyroxyl and the carbon of SAM methyl group (*d4*) in SpnI-RAGL complex (4.45 ± 0.35 Å and 3.33 ± 0.28 Å) is shorter than the corresponding distances in SpnI-**II** complex (5.03 ± 0.63 Å and 4.58 ± 0.82 Å). The substrate binding pockets of SpnK and SpnI were similar. Sequence alignment of rhamnose O-MTs shows that the Asp299/Asp306 is highly conserved while Trp301/Gln 308 is optional and likely correlated to the specific substrate (Figs. S6, S7). Rhamnose 2′-O-MTs contain a DLQT motif while rhamnose 3′-O-MTs contain s DLWT motif. The large side chain of tryptophan in SpnK likely reduces the space available to accommodate the substrate and pushes the 3′-OH of the substrate toward the catalytic histidine (Fig. S8).

3.5. Binding free energy analysis

In vitro experiments have shown that despite the minor difference of one hydroxyl group among most of the substrates mentioned earlier, they performed varying degrees of binding affinity toward SpnK and SpnI. To assess the precision of MD simulations, the MMPBSA tool was employed to calculate the binding free energy of SpnK- RAGL, SpnK-**I**, SpnK-**III**, SpnI-RAGL and SpnI-**II** complexes. Various types of energy that contribute to binding, for example, van der Waals interactions, electrostatic interactions, polar and non-polar solvation interactions, were calculated, and their average values are summarized in Table S5. Examination of the binding free energy of SpnK complexes indicated that compound **I** exhibited the most potent binding free energy of −20.9 kcal/mol, confirming its high affinity toward SpnK, surpassing that of RAGL with a binding free energy of −17.91 kcal/mol. On the other hand, the non-substrate, compound III, exhibited the highest binding free energy of −10.04 kcal/mol, in accordance with experimental findings. Investigation of the binding free energy of SpnI complexes revealed that RAGL exhibited lower binding free energy of −31.25 kcal/mol, which was inferior to the non-substrate, compound **II**, with a binding free energy of −12.04 kcal/mol, consistent with experimental observations. Notably, the binding free energy of RAGL was also lower in SpnI than in SpnK.

4. Discussion

The sequential catalysis of OMTs is observed in the post glycosylation modification steps in biosynthesis of many secondary metabolites. Analysis reveals that SpnI and SpnK exhibit sequence similarities to ElmMI, ElmMII, TylE (demethylmacrocin 2′-O-MT) and MycE (Fig. S9). In contrast, SpnH shows sequence similarity to ElmMIII (demethylelloramycin A rhamnose 4′-O-MT), TylF (macrocin 3′-O-MT) and MycF (mycinamicin III javose 3′-O-MT) (Fig. S10) [41,42].

It can be deduced from the strict methylation order that *O*-methylation catalyzed by O-MTs from MycE/TylE family is the prerequisite for the subsequent *O*-methylation catalyzed by O-MTs from MycF/TylF family [42,43]. ElmMI, ElmMII and ElmMIII exhibit strict biosynthetic

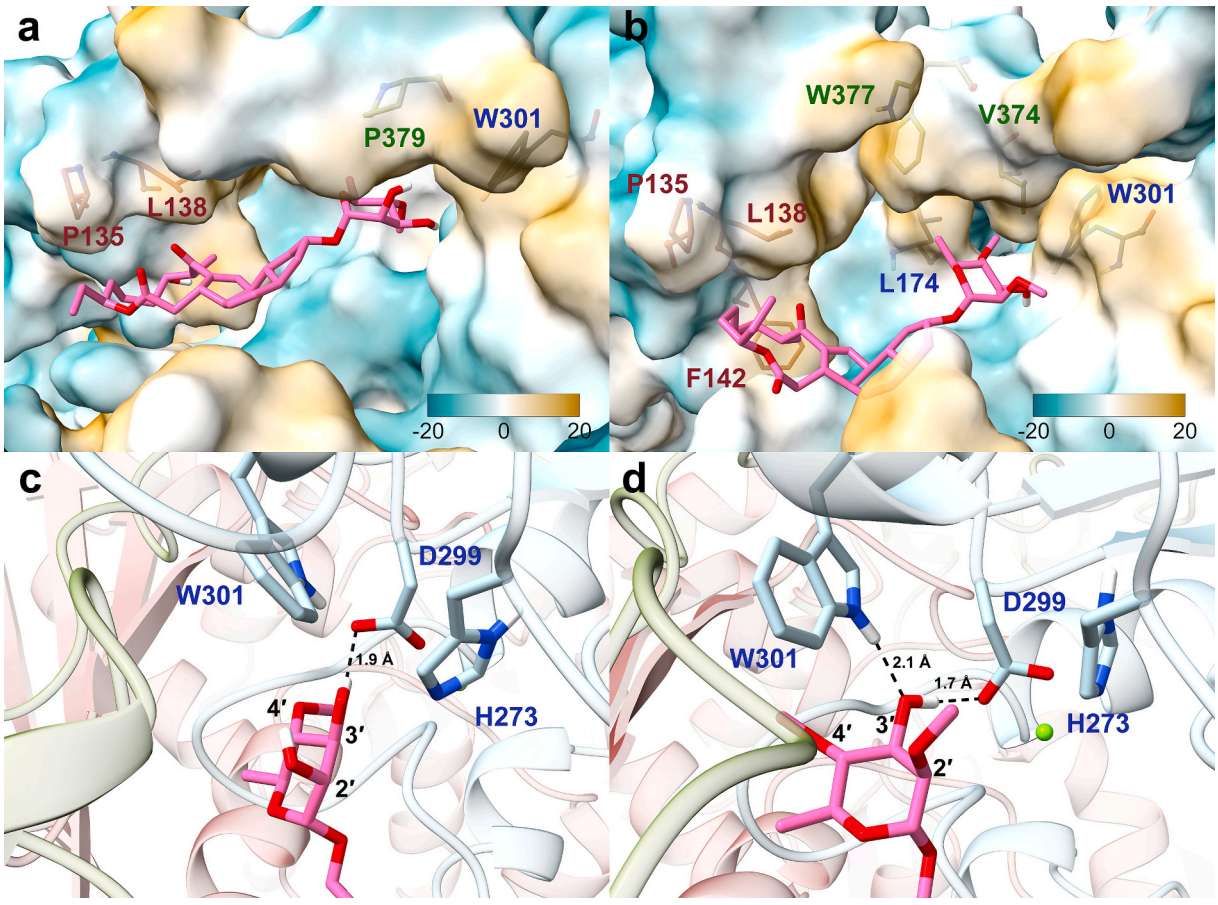

Fig. 4. MD simulations of SpnK and non-substrates. (a, b) Hydrophobicity surface representation of **III** (a) and **V** (b) binding pocket. Residues participated in hydrophobic interactions are depicted as sticks. **III** as well as **V** are shown in magenta sticks. (c, d) Residues involved in non-substrate **III** (c) and V (d) recognition are depicted as sticks, hydrogen bonds are donated by black dashed lines.

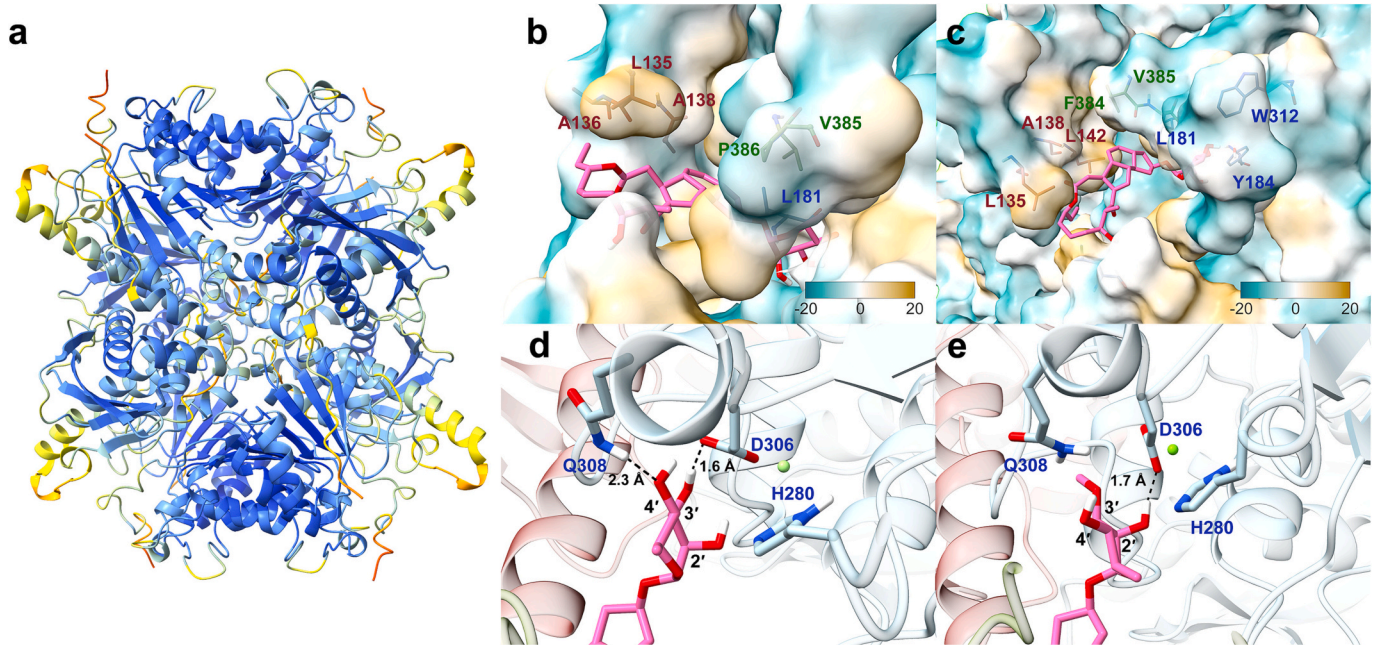

Fig. 5. Aspartate constrains substrates binding in SpnI. (a) Ribbon diagram of SpnI tetramer predicted with AlphaFold Multimer and colored by per-residue pLDDT scores. A light spectrum from red to blue corresponds to lowest to highest pLDDT scores, respectively. (b, c) Hydrophobicity surface representation of RAGL (b) and **II** (c) binding pocket. Residues participated in hydrophobic interactions are depicted as sticks. (d, e) Residues involved in substrate RAGL (d) and non-substrate **II** (e) recognition are depicted as sticks, hydrogen bonds are donated by black dashed lines.

sequence in the methylation of rhamnose 2′-, 3′- and 4′-hydroxyl moieties. ElmMIII efficiently methylates only elloramycin derivatives that already possess at least one methoxy group either at C2′ or C3′. Moreover, 3′-methyoxy group enhances ElmMIII efficiency. *In vitro* analysis reveals that ElmMI catalyzes unmethylated rhamnosyl-tetracenomycin C much better than ElmMII, implying that the catalysis sequence follows the order of ElmMI, ElmMII, and ElmMIII [41]. Although MycF could recognize mycinamicin VI, a substrate of 2′-OMT MycE, and convert roughly 10 % of it to 3′-methoxy-mycinamicin VI at high concentrations, the substrate selectivity of MycE is more stringent. Therefore, MycE is unable to produce double-methylated mycinamicin VI from 3′-methoxy-mycinamicin VI, consistent with the observation in SpnK [44]. But in the case of methylation of the tylosin 6-deoxy-D-allose moiety, the substrate flexibility of TylE as well as TylF is exceptional. TylF overexpression conditions allow for *in vitro* interchange of *O*-methylation sequence catalyzed by TylE and then TylF. Purified recombinant TylF can methylate 3′-OH of demethyllactenocin or demethylmacrocin, which precedes the 2′-*O*-methylation catalyzed by TylE. Additionally, TylE can recognize the 3′-*O*-methylated substrates, 2′-*O*-demethyldesmycosin or 2′-*O*-demethyltylosin [45].

The SpnK structure reported here represents the first example of an O-MT catalyzing the 3′-*O*-methylation from the MycE/TylE family. Consistent with the unique features observed in the MycE structure, SpnK also consists of four identical tetrahedrally arranged subunits, of which three subunits form one complete substrate binding pocket. The detailed structural analysis of SpnK catalyzing the second *O*-methylation reaction in the modification of rhamnose moiety, sheds light on the structural feature that governs the strict order of 2′-, 3′- and 4′-OH methylation in the biosynthesis of spinosad. Notably, SpnK can accommodate 2′-methoxyl groups in the active site but cannot accommodate 4′-methoxyl group. Based on the structure of SpnK, we speculate that the methylation of 4′-OH act as a barrier for the 3′-*O*-methylation. Docking results and MD simulations suggest that Asp299 and Trp301 are likely the moderators of substrate binding. When the native substrate RAGL or **I** fit into the active site, Asp299 stabilizes the 4′-OH through a hydrogen bond. If the 4′-OH has already been methylated, as the case of **III** or **V** binding, the network of interaction changes. A new hydrogen bond is formed between Trp301 and 3′-OH. Hydrogen bond between Asp299 and the rhamnose moiety shifts from the 4′-OH to 3′-OH, thus orienting the sugar ring. The 3′-OH is found pointing away from active site His273 because of inward rotation of sugar ring, resulting in the loss of activity toward 4′-methoxylated substrates. The sequence alignment of rhamnose O-MTs of MycE/TylE family unravels the potential role of the conserved aspartate in directing the regioselectivity of these enzymes.

Comparison between SpnK and SpnI also highlights the functional significance of the conserved aspartate which plays a vital role of stabilizing adjacent hydroxyl group. Substrate selectivity and activity of SpnI can be attributed to the hydrogen bond between 3′-OH and Asp306. Side chain difference between glutamine and tryptophan might influence the rotational freedom of the rhamnose moiety and restrict the hydroxyl group to be methylated. The remarkable association between the regiospecificity of enzymes and the presence of specific amino acids bears immense significance and promises to serve as a valuable tool in elucidating and annotating unexplored biosynthetic pathways for natural products.

Compared to SpnI and SpnK, SpnH exhibits a promiscuous behavior and can accommodate all four substrates (Scheme 1). Mechanistically, while SpnI and SpnK are members of the MycE/TylE family and utilize a histidine as the catalytic residue, SpnH belongs to MycF/TylF family using an aspartate to deprotonate the hydroxyl group. It's conceivable that the diverse substrate selectivity observed among these enzymes arises from differences in their active site architectures. The crystal structure of SpnH with SAH has been reported (PDB code: 4CE0), revealing that unlike SpnK, SpnH functions as a monomer. The unstructured region (residue 22–45) situated between α1 and α2 of SpnH may potentially have a crucial function in substrate recognition. The proposed catalytic residue, Asp187, is in proximity to Mg^{2+}, and may coordinate with the 2′- or 3′-oxygens of the substrate.

Understanding molecular basis for regioselectivity of *O*-methyltransferase is important to modifying the substrate selectivity and engineering of novel biosynthetic products. O-MTs from MycE/TylE family show flexibility in the macrolide ring part of the substrate and strict constraint on the sugar ring. In this study, we have gained new insights into the substrate recognition and binding mechanisms of MycE/TylE family O-MTs, providing a foundation for future engineering endeavors. Understanding the architecture of active site and substrate specificity mechanisms can pave the way for the development of more efficient and selective O-MTs for biosynthesis of complex natural products. With the aid of structural information on sugar O-MTs and methionine adenosyltransferases, these enzymes could be optimized further and potentially utilized in the enzymatic synthesis of novel complex natural product analogues.

CRediT authorship contribution statement

Shuxin Huang: Conceptualization, Methodology, Data analysis, Validation, Writing – original draft. Huining Ji: Data analysis, Validation. Jianting Zheng: Conceptualization, Supervision, Writing – review & editing, Funding acquisition.

Declaration of competing interest

The authors declare that they have no known competing financial interests or personal relationships that could have appeared to influence the work reported in this paper.

Data availability

Atomic coordinates and structures factors of SpnK and SpnK-SAH have been deposited to PDB with accession codes 8IA9 and 8IAA, respectively.

Acknowledgments

This work was supported by National Key Research and Development Program of China (2020YFA0907900) and National Natural Science Foundation of China (32070040, 32370071). We thank beamlines BL18U1 at Shanghai Synchrotron Radiation Facility for diffraction data collection.

Appendix A. Supplementary data

Supplementary data to this article can be found online at https://doi.org/10.1016/j.ijbiomac.2023.126763.

References

[1] D.K. Liscombe, G.V. Louie, J.P. Noel, Architectures, mechanisms and molecular evolution of natural product methyltransferases, Nat. Prod. Rep. 29 (10) (2012) 1238–1250, https://doi.org/10.1039/C2NP20029E.
[2] M. Tomkuvienė, M. Mickutė, G. Vilkaitis, S. Klimašauskas, Repurposing enzymatic transferase reactions for targeted labeling and analysis of DNA and RNA, Curr. Opin. Biotechnol. 55 (2019) 114–123, https://doi.org/10.1016/j.copbio.2018.09.008.
[3] R.Z. Jurkowska, A. Jeltsch, Mechanisms and biological roles of DNA methyltransferases and DNA methylation: from past achievements to future challenges, in: A. Jeltsch, R.Z. Jurkowska (Eds.), DNA Methyltransferases - Role and Function, Springer International Publishing, Cham, 2016, pp. 1–17, https://doi.org/10.1007/978-3-319-43624-1_1.
[4] B.J.C. Law, A.-W. Struck, M.R. Bennett, B. Wilkinson, J. Micklefield, Site-specific bioalkylation of rapamycin by the RapM 16-O-methyltransferase, Chem. Sci. 6 (5) (2015) 2885–2892, https://doi.org/10.1039/C5SC00164A.
[5] E. Jalali, J.S. Thorson, Enzyme-mediated bioorthogonal technologies: catalysts, chemoselective reactions and recent methyltransferase applications, Curr. Opin. Biotechnol. 69 (2021) 290–298, https://doi.org/10.1016/j.copbio.2021.02.010.

[6] H.L. Schubert, R.M. Blumenthal, X. Cheng, Many paths to methyltransfer: a chronicle of convergence, Trends Biochem. Sci. 28 (6) (2003) 329–335, https://doi.org/10.1016/S0968-0004(03)00090-2.
[7] J.-L. Ferrer, C. Zubieta, R.A. Dixon, J.P. Noel, Crystal structures of alfalfa caffeoyl coenzyme A 3-O-methyltransferase, Plant Physiol. 137 (3) (2005) 1009–1017, https://doi.org/10.1104/pp.104.048751.
[8] T.D. Huber, B.R. Johnson, J. Zhang, J.S. Thorson, AdoMet analog synthesis and utilization: current state of the art, Curr. Opin. Biotechnol. 42 (2016) 189–197, https://doi.org/10.1016/j.copbio.2016.07.005.
[9] C. Dalhoff, G. Lukinavičius, S. Klimašauskas, E. Weinhold, Direct transfer of extended groups from synthetic cofactors by DNA methyltransferases, Nat. Chem. Biol. 2 (1) (2006) 31–32, https://doi.org/10.1038/nchembio754.
[10] M.R. Bennett, S.A. Shepherd, V.A. Cronin, J. Micklefield, Recent advances in methyltransferase biocatalysis, Curr. Opin. Chem. Biol. 37 (2017) 97–106, https://doi.org/10.1016/j.cbpa.2017.01.020.
[11] X. Wang, C. Wang, L. Duan, L. Zhang, H. Liu, Y.-m. Xu, Q. Liu, T. Mao, W. Zhang, M. Chen, M. Lin, A.A.L. Gunatilaka, Y. Xu, I. Molnár, Rational reprogramming of O-methylation regioselectivity for combinatorial biosynthetic tailoring of benzenediol lactone scaffolds, J. Am. Chem. Soc. 141 (10) (2019) 4355–4364, https://doi.org/10.1021/jacs.8b12967.
[12] N. Koirala, N.H. Thuan, G.P. Ghimire, D.V. Thang, J.K. Sohng, Methylation of flavonoids: chemical structures, bioactivities, progress and perspectives for biotechnological production, Enzyme Microb. Technol. 86 (2016) 103–116, https://doi.org/10.1016/j.enzmictec.2016.02.003.
[13] H.A. Kirst, K.H. Michel, J.S. Mynderase, E.H. Chio, R.C. Yao, W.M. Nakasukasa, L. D. Boeck, J.L. Occlowitz, J.W. Paschal, J.B. Deeter, G.D. Thompson, Discovery, Isolation, and Structure Elucidation of a Family of Structurally Unique, Fermentation-Derived Tetracyclic Macrolides, Synthesis and Chemistry of Agrochemicals III, American Chemical Society, 1992, pp. 214–225, https://doi.org/10.1021/bk-1992-0504.ch020.
[14] P.L. McCormack, Spinosad: in pediculosis capitis, Am. J. Clin. Dermatol. 12 (5) (2011) 349–353, https://doi.org/10.2165/11208070-000000000-00000.
[15] C. Waldron, P. Matsushima, P.R. Rosteck, M.C. Broughton, J. Turner, K. Madduri, K.P. Crawford, D.J. Merlo, R.H. Baltz, Cloning and analysis of the spinosad biosynthetic gene cluster of *Saccharopolyspora spinosa*, Chem. Biol. 8 (5) (2001) 487–499, https://doi.org/10.1016/S1074-5521(01)00029-1.
[16] H.J. Kim, J.A. White-Phillip, Y. Ogasawara, N. Shin, E.A. Isiorho, H.-w. Liu, Biosynthesis of Spinosyn in Saccharopolyspora spinosa: synthesis of permethylated rhamnose and characterization of the functions of SpnH, SpnI, and SpnK, Journal of the American Chemical Society 132 (9) (2010) 2901–2903, https://doi.org/10.1021/ja910223x.
[17] T.C. Sparks, G.D. Crouse, J.E. Dripps, P. Anzeveno, J. Martynow, C.V. DeAmicis, J. Gifford, Neural network-based QSAR and insecticide discovery: spinetoram, J. Comput. Aided Mol. Des. 22 (6) (2008) 393–401, https://doi.org/10.1007/s10822-008-9205-8.
[18] T.C. Sparks, G.D. Crouse, Z. Benko, D. Demeter, N.C. Giampietro, W. Lambert, A. V. Brown, The spinosyns, spinosad, spinetoram, and synthetic spinosyn mimics - discovery, exploration, and evolution of a natural product chemistry and the impact of computational tools, Pest Manag. Sci. 77 (8) (2021) 3637–3649, https://doi.org/10.1002/ps.6073.
[19] P. Emsley, B. Lohkamp, W.G. Scott, K. Cowtan, Features and development of Coot, Acta Crystallogr. Sect. D 66 (4) (2010) 486–501, https://doi.org/10.1107/S0907444910007493.
[20] M.D. Winn, C.C. Ballard, K.D. Cowtan, E.J. Dodson, P. Emsley, P.R. Evans, R. M. Keegan, E.B. Krissinel, A.G.W. Leslie, A. McCoy, S.J. McNicholas, G. N. Murshudov, N.S. Pannu, E.A. Potterton, H.R. Powell, R.J. Read, A. Vagin, K. S. Wilson, Overview of the CCP4 suite and current developments, Acta Crystallographica Section D 67 (4) (2011) 235–242, https://doi.org/10.1107/S0907444910045749.
[21] T.D. Goddard, C.C. Huang, E.C. Meng, E.F. Pettersen, G.S. Couch, J.H. Morris, T. E. Ferrin, UCSF ChimeraX: meeting modern challenges in visualization and analysis, Protein Sci. 27 (1) (2018) 14–25, https://doi.org/10.1002/pro.3235.
[22] L.L.C. Schrodinger, The PyMOL molecular graphics system, Version 1 (8) (2015).
[23] E. Richard, O.N. Michael, P. Alexander, A. Natasha, S. Andrew, G. Tim, Ž. Augustin, B. Russ, B. Sam, Y. Jason, R. Olaf, B. Sebastian, Z. Michal, B. Alex, P. Anna, C. Andrew, T. Kathryn, J. Rishub, C. Ellen, K. Pushmeet, J. John, H. Demis, Protein complex prediction with AlphaFold-Multimer, bioRxiv (2021), https://doi.org/10.1101/2021.10.04.463034.
[24] O. Trott, A.J. Olson, AutoDock Vina: improving the speed and accuracy of docking with a new scoring function, efficient optimization, and multithreading, J. Comput. Chem. 31 (2) (2010) 455–461, https://doi.org/10.1002/jcc.21334.
[25] R. Anandakrishnan, B. Aguilar, A.V. Onufriev, H++ 3.0: automating pK prediction and the preparation of biomolecular structures for atomistic molecular modeling and simulations, Nucl. Acids Res. 40 (W1) (2012) W537–W541, https://doi.org/10.1093/nar/gks375.
[26] M.J. Frisch, G.W. Trucks, H.B. Schlegel, G.E. Scuseria, M.A. Robb, J.R. Cheeseman, G. Scalmani, V. Barone, B. Mennucci, G.A. Petersson, M. Caricato, H. Nakatsuji, M. Caricato, X. Li, H.P. Hratchian, A.F. Izmaylov, J. Bloino, G. Zheng, M. Hada, M. Ehara, K. Toyota, R. Fukuda, J. Hasegawa, M. Ishida, T. Nakajima, Y. Honda, O. Kitao, H. Nakai, T. Vreven, J.A. Montgomery Jr., J.E. Peralta, F. Ogliaro, M. J. Bearpark, J.J. Heyd, E.N. Brothers, K.N. Kudin, V.N. Staroverov, R. Kobayashi, J. Normand, K. Raghavachari, A.P. Rendell, J.C. Burant, S.S. Iyengar, J. Tomasi, M. Cossi, J.M. Millam, M. Klene, J.E. Knox, J.B. Cross, V. Bakken, C. Adamo, J. Jaramillo, R. Gomperts, R.E. Stratmann, O. Yazyev, A.J. Austin, R. Cammi, C. Pomelli, J.W. Ochterski, R.L. Martin, K. Morokuma, V.G. Zakrzewski, G.A. Voth, P. Salvador, J.J. Dannenberg, S. Dapprich, A.D. Daniels, O. Farkas, J.B. Foresman, J.V. Ortiz, J. Cioslowski, D.J. Fox, Gaussian 09, Gaussian Inc., Wallingford CT, 2009.
[27] W.D. Cornell, P. Cieplak, C.I. Bayly, I.R. Gould, K.M. Merz, D.M. Ferguson, D. C. Spellmeyer, T. Fox, J.W. Caldwell, P.A. Kollman, A second generation force field for the simulation of proteins, Nucleic Acids, and Organic Molecules, Journal of the American Chemical Society 117 (19) (1995) 5179–5197, https://doi.org/10.1021/ja00124a002.
[28] D. Case, I. Ben-Shalom, S.R. Brozell, D.S. Cerutti, T. Cheatham, V.W.D. Cruzeiro, T. Darden, R. Duke, D. Ghoreishi, M. Gilson, H. Gohlke, A. Götz, D. Greene, R. Harris, N. Homeyer, Y. Huang, S. Izadi, A. Kovalenko, T. Kurtzman, P. A. Kollman, Amber, University of California, San Francisco. 2018 (2018).
[29] J.A. Maier, C. Martinez, K. Kasavajhala, L. Wickstrom, K.E. Hauser, C. Simmerling, ff14SB: improving the accuracy of protein side chain and backbone parameters from ff99SB, J. Chem. Theory Comput. 11 (8) (2015) 3696–3713, https://doi.org/10.1021/acs.jctc.5b00255.
[30] T. Darden, D. York, L. Pedersen, Particle mesh Ewald: an *N*·log(*N*) method for Ewald sums in large systems, J. Chem. Phys. 98 (12) (1993) 10089–10092, https://doi.org/10.1063/1.464397.
[31] J.-P. Ryckaert, G. Ciccotti, H.J.C. Berendsen, Numerical integration of the Cartesian equations of motion of a system with constraints: molecular dynamics of n-alkanes, J. Comput. Phys. 23 (3) (1977) 327–341, https://doi.org/10.1016/0021-9991(77)90098-5.
[32] D.R. Roe, T.E. Cheatham III, PTRAJ and CPPTRAJ: software for processing and analysis of molecular dynamics trajectory data, J. Chem. Theory Comput. 9 (7) (2013) 3084–3095, https://doi.org/10.1021/ct400341p.
[33] W. Humphrey, A. Dalke, K. Schulten, VMD: visual molecular dynamics, J. Mol. Graph. 14 (1) (1996) 33–38, https://doi.org/10.1016/0263-7855(96)00018-5.
[34] B.R. Miller III, T.D. McGee Jr., J.M. Swails, N. Homeyer, H. Gohlke, A.E. Roitberg, MMPBSA. py: an efficient program for end-state free energy calculations, J. Chem. Theory Comp. 8 (9) (2012) 3314–3321, https://doi.org/10.1021/ct300418h.
[35] P.A. Kollman, I. Massova, C. Reyes, B. Kuhn, S. Huo, L. Chong, M. Lee, T. Lee, Y. Duan, W. Wang, O. Donini, P. Cieplak, J. Srinivasan, D.A. Case, T.E. Cheatham, Calculating structures and free energies of complex molecules: combining molecular mechanics and continuum models, Acc. Chem. Res. 33 (12) (2000) 889–897, https://doi.org/10.1021/ar000033j.
[36] L. Holm, P. Rosenstrom, Dali server: conservation mapping in 3D, Nucl. Acids Res. 38 (suppl_2) (2010) W545–W549, https://doi.org/10.1093/nar/gkq366.
[37] D.L. Akey, S. Li, J.R. Konwerski, L.A. Confer, S.M. Bernard, Y. Anzai, F. Kato, D. H. Sherman, J.L. Smith, A new structural form in the SAM/metal-dependent O-methyltransferase family: MycE from the mycinamicin biosynthetic pathway, J. Mol. Biol. 413 (2) (2011) 438–450, https://doi.org/10.1016/j.jmb.2011.08.040.
[38] R. Park, C. Ongpipattanakul, S.K. Nair, A.A. Bowers, B. Kuhlman, Designer installation of a substrate recruitment domain to tailor enzyme specificity, Nat. Chem. Biol. (2022), https://doi.org/10.1038/s41589-022-01206-0.
[39] N. Sokolova, L. Zhang, S. Deravi, R. Oerlemans, M.R. Groves, K. Haslinger, Structural characterization and extended substrate scope analysis of two Mg2+-dependent O-methyltransferases from bacteria**, ChemBioChem 24 (9) (2023), e202300076, https://doi.org/10.1002/cbic.202300076.
[40] D. Chatterjee, D. Kudlinzki, V. Linhard, K. Saxena, U. Schieborr, S.L. Gande, J. P. Wurm, J. Wöhnert, R. Abele, V.V. Rogov, V. Dötsch, H.D. Osiewacz, S. Sreeramulu, H. Schwalbe, Structure and biophysical characterization of the S-adenosylmethionine-dependent O-methyltransferase PaMTH1, a putative enzyme accumulating during senescence of Podospora anserina*, J. Biol. Chem. 290 (26) (2015) 16415–16430, https://doi.org/10.1074/jbc.M115.660829.
[41] E.P. Patallo, G. Blanco, C. Fischer, A.F. Braña, J. Rohr, C. Méndez, J.A. Salas, Deoxysugar methylation during biosynthesis of the antitumor polyketide elloramycin by Streptomyces olivaceus: characterization of three methyltransferase genes*, J. Biol. Chem. 276 (22) (2001) 18765–18774, https://doi.org/10.1074/jbc.M101225200.
[42] S. Li, Y. Anzai, K. Kinoshita, F. Kato, D.H. Sherman, Functional analysis of MycE and MycF, two O-methyltransferases involved in the biosynthesis of mycinamicin macrolide antibiotics, ChemBioChem 10 (8) (2009) 1297–1301, https://doi.org/10.1002/cbic.200900088.
[43] A.J. Kreuzman, J.R. Turner, W.K. Yeh, Two distinctive O-methyltransferases catalyzing penultimate and terminal reactions of macrolide antibiotic (tylosin) biosynthesis. Substrate specificity, enzyme inhibition, and kinetic mechanism, J. Biol. Chem. 263 (30) (1988) 15626–15633, https://doi.org/10.1016/S0021-9258(19)37634-3.
[44] S.M. Bernard, D.L. Akey, A. Tripathi, S.R. Park, J.R. Konwerski, Y. Anzai, S. Li, F. Kato, D.H. Sherman, J.L. Smith, Structural basis of substrate specificity and regiochemistry in the MycF/TylF family of sugar O-methyltransferases, ACS Chem. Biol. 10 (5) (2015) 1340–1351, https://doi.org/10.1021/cb5009348.
[45] E. Kim, M.C. Song, M.S. Kim, J.Y. Beom, E.Y. Lee, D.-M. Kim, S.-J. Nam, Y.J. Yoon, Characterization of the two methylation steps involved in the biosynthesis of mycinose in tylosin, J. Nat. Prod. 79 (8) (2016) 2014–2021, https://doi.org/10.1021/acs.jnatprod.6b00267.